Intrinsic multi-valley and multi-bandgap absorption and inhibition of exciton formation in hybrid perovskites

Jacky Even, Laurent Pedesseau, Claudine Katan

Intrinsic multi-valley and multi-bandgap absorption and inhibition of exciton formation in hybrid perovskites

Jacky Even[1]*, Laurent Pedesseau[1] & Claudine Katan[2]*

[1]Université Européenne de Bretagne, INSA FOTON UMR 6082, 35708 Rennes, France.

[2]CNRS, Institut des Sciences Chimiques de Rennes UMR6226, 35042 Rennes, France

*Correspondence to: jacky.even@insa-rennes.fr, Claudine.katan@univ-rennes1.fr

Abstract: Solution-processable metal-halide perovskites recently opened a new route towards low-cost manufacture of photovoltaic cells. Converting sunlight into electrical energy depends on several factors among which a broad absorption across the solar spectrum and attractive charge transport properties are of primary importance. Hybrid perovskites meet such prerequisites but, despite foremost experimental research efforts, their understanding remains scanty. In addition, the toxicity of lead may restrict market clearance. Here we show that in these materials, the appropriate absorption and transport properties are afforded by the multi-bandgap and multi-valley nature of their band structure. We also investigate the nature of the photoexcited species and evidence exciton screening by collective orientational motion of the organic cations at room temperature. We introduce related dressed quasiparticules to discuss carrier mobility. Chlorine doping hinders such collective motions, leading to improved light-harvesting and transport. We further suggest $CH_3NH_3SnI_{3-x}Br_x$ as a good alternative to circumvent toxicity.

In a photovoltaic (PV) device, the conversion efficiency of solar radiation into electrical power is paramount. In 1961, Shockley and Queisser established the theoretical efficiency limit of an ideal single p-n junction solar cell, based on the principle of detailed balance[1]. This limit of 33.7% is almost attained by the best-performing heterojunctions. Among the strategies developed to bypass this limit, concentrated multi-junction (multiple p-n junctions) PV cells[2,3] undeniably afford upmost conversion efficiencies[2] but at the expense of elaborate and expensive growth modus operandi. Conversely, solution-processable metal-halide perovskites have recently opened a new route towards low-cost manufacture of solar cells. The tremendous research effort conducted during the last 2 years has mainly focused on the methylammonium lead-iodide perovskite ($CH_3NH_3PbX_3$, X=I). First used as the sensitizer in conventional dye sensitized solar cells[4-6], thanks to its good light harvesting abilities, its attractive charge transport properties allowed to achieve Meso-Superstructured Solar Cells (MSSC) and solid thin-film planar heterojunctions with record efficiencies up to 15% (ref. 7-15). In fact, broad absorption across the solar spectrum and appropriate electron and/or hole mobilities are prerequisites to high solar-to-electrical power conversion efficiencies. While there is clear experimental evidence that lead-halide perovskites meet these conditions, the understanding of underlying mechanism remains scarce[14-16]. As Loi and Hummelen put forward, "*it is now time to investigate the physical properties that make hybrid perovskites so promising for solar-energy conversion*"[16]. First, the origin of the favorable light absorption over the visible to near-IR range is still mysterious in spite of a couple of recent theoretical investigations[17-23]. At room temperature, the linear absorption spectrum of $CH_3NH_3PbI_3$ shows two absorption peaks located at 760 and 480 nm (ref. 14, 15). Whereas the low energy peak was attributed to the direct bandgap transition from the

valence band (VB) maximum to the conduction band (CB) minimum, the origin of the high-energy peak is clearly unresolved[15]. Moreover, a hot hole cooling mechanism was also suggested for the intra-band relaxation after optical excitation at high energy for $CH_3NH_3PbI_3$ (ref. 15). Besides, halogen substitution ($X_3=I_{3-x}Cl_x$ or $I_{3-x}Br_x$) has shown to provide improved transport properties and cell stability while preserving good performances including low fundamental energy losses[5,11-14]. To understand such improvements, Snaith and colleagues have recently thoroughly investigated the carrier dynamics after optical excitation for $X_3=I_{3-x}Cl_x$ (ref. 24). It is shown that after photoexcitation the second order transient THz transmission dynamics of triiodide compounds is an order of magnitude faster than for the mixed halide. Moreover, the latter exhibit larger mobilities (+43%), sizeable enhancement of the absorption above the bandgap and a threefold increase of the photoluminescence radiative lifetime[24]. Snaith and colleagues suggest localization of electrons and holes in different regions of the perovskite's unit cell but do not rule out the presence of excitons in the material following photoexcitation[24]. Thus, it is still unclear whether the photoexcited species are excitons or free charges. Moreover, little is known about what makes mixed halides superior to triiodide perovskites, namely the origin of increased mobilities and decreased charge carrier recombinations that enhance PV efficiencies. Last, the high percentage of lead might be a problem for future development regarding European Directives on the use of hazardous substances in electrical and electronic equipment[25].

Here we report a theoretical investigation of a series of metal-halide perovskites: $CH_3NH_3MX_3$, X=I, Br, Cl and M=Pb, Sn, Ge. First, we thoroughly analyse calculated absorption spectra of the *reference* cubic phase of lead-based compounds. Next, we discuss the nature of the photoexcited species based on extensive use of both recent and older experimental findings, namely temperature dependent absorption spectra[26] and millimetre-wave spectroscopy[27], low frequency

dielectric measurements[28], and NMR data related to the motion of molecular cations[29]. Then we discuss in sequence the impact of halogen substitution on absorption and carrier mobilities. Last, we consider replacement of lead by tin[18,30] as an option to address environmental issues. Computational details are provided as Supplementary Informations.

The ideal cubic crystal structure (Pm3m space group) of metal-halide perovskites is sketched Fig. 1a together with the corresponding Brillouin Zone (BZ) in reciprocal space (Fig. 1b). The latter has high symmetry points among which the R and M are of major importance to our purpose. In fact, recent calculations of the imaginary part of the dielectric function for the high temperature cubic phase of $CH_3NH_3PbI_3$, based on density functional theory (DFT) within the Random-Phase Approximation (RPA), evidenced the onsets of primary and secondary absorptions related to R and M points, respectively[18]. Similar features are obtained for $CH_3NH_3PbCl_3$ (Supplementary Fig. S1). These calculations do not consider spin-orbit coupling (SOC) that induces giant splittings of the CB of lead-based hybrid perovskites[17,18,31]. A first insight in these optical features can be gained from group theory. The symmetry analysis of the electronic states at R and M in the simple (without SOC) and double (with SOC) group allows identifying the optically allowed transitions. The simple group T_{1u} vectorial representation of the CB at R is splitted in a doubly degenerated $E_{1/2u}$ (spin-orbit split-off states) and a fourfold degenerated $F_{3/2u}$ state (Fig. 1c). The ground state isotropic optical transition is thus predicted at R between doubly degenerated $E_{1/2g}$ VB and $E_{1/2u}$ CB states depicted Fig. 1d for the calculated band structure. Complete diagrams with and without SOC are provided in Supplementary Fig. S1 and S2. At R, a series of other transitions are optically allowed, the lowest in energy corresponding to two secondary transitions $F_{3/2g} \rightarrow E_{1/2u}$ and $E_{1/2g} \rightarrow F_{3/2u}$ (Fig. 1). The transition between the doubly degenerated $E_{1/2g}$ VB and $E_{1/2u}$ CB states at M is also optically allowed and transverse electric (TE). To determine

which of these transitions is responsible for the peak experimentally observed at 480nm in the absorption spectra, we evaluate the strength of the optical transitions, as defined by $\frac{2}{m_e}|\langle\psi_{CB}|-i\hbar\nabla|\psi_{VB}\rangle|^2$ (Supplementary Table S3 and S4). Values are significantly larger for M, thanks to a threefold contribution, and the upwards 1eV energy shift is consistent with experimental findings. The threefold contribution can be intuited from the Fermi surface plotted in the first BZ close to the top of the VB (Fig. 1e). Moreover, the different optically allowed transitions have sizeable matrix elements disclosing the multi-bandgap nature at the origin of broad absorption of $CH_3NH_3PbI_3$, expanding from the visible to the near-IR (see also additional text in Supplementary).

Next, the Fermi surface (Fig. 1e) reveals clear connection between R and M along the edges of the BZ. While the BZ valleys are located around R, M correspond to saddle points. This suggests that, in reciprocal space, carriers generated by optical absorption at M and all along the M→R paths at various wavelengths (Fig. 1d) can flow easily towards R. The relaxation process may be assisted by acoustic phonons or coupling to collective molecular rotations (vide infra). Contrarily, one expects that some of the carriers generated by the secondary optical transitions at R may be trapped in the $F_{3/2u}$ (CB) and $F_{3/2g}$ (VB) states (Fig. 1d). Further relaxation $F_{3/2g} \rightarrow E_{1/2g}$ (holes) and $F_{3/2u} \rightarrow E_{1/2u}$ (electrons) may occur by optical phonons assisted relaxations, provided that the energy conservation rule is fulfilled. Such a "phonon bottleneck" is well known in the case of carrier injection in semiconductor quantum dots[32,33]. However, in quantum dots, carrier assisted (Auger relaxation) is the dominant effect in the high injection regime, yielding very fast carrier relaxation. A similar hot hole cooling (intra-band process) from $F_{3/2g}$ to $F_{1/2g}$ is consistent with the relaxation after optical excitation reported for $CH_3NH_3PbI_3$ (ref. 15). Similar results are obtained for the cubic Pm3m phase of $CH_3NH_3PbCl_3$ (Supplementary Fig. S3 and Table S5 and

S6), with a larger bandgap and a larger splitting between primary (R) and secondary (M) optical transitions.

Let's know discuss about the nature of the photoexcited species at room temperature. If experimental studies clearly exhibit excitonic effects in the low-energy part of the absorption spectra of $CH_3NH_3PbX_3$ at low temperatures[34,35] (LT), things remain unclear at room temperature[24] (RT). For the secondary transition at M, excitonic effects are expected to be small as a consequence of its saddle point nature (Fig. 1d,e). This is consistent with the absence of excitonic features at higher energy in the spectrum recorded at 4.2 K (Ref. 34). Theoretically, excitonic effects can be accounted for using the Bethe-Salpeter Equation (BSE) starting from the monoelectronic states calculated at the DFT level. Enhancement of absorption at the bandgap is predicted both for $CH_3NH_3PbCl_3$ (Supplementary Fig. S4) and $CH_3NH_3PbI_3$ (ref. 18) in their cubic phases. But, in the perturbative BSE approach, screening of the electron-hole interaction due to atomic motion is not taken into account. To gauge the importance and origin of screening we may go back to experimental data recorded two decades ago. Ishihara et al. reported absorption spectra of $CH_3NH_3PbI_3$ at different temperatures[26]. These data are consistent with an exciton quenching between 159K and 212K (Fig. 2), in relation with the structural transition at T_c=162K. This exciton quenching includes both exciton screening and gap-switching[17,18] (ill-named exciton-switching), that also appears in 2D hybrids[26,36] (see supplementary for additional discussion). A convenient way to simulate exciton screening is to consider two-particle wave function and effective mass equations for electron and hole[37]. The energy and absorption of the excitonic bound states are related to the Rydberg energy of the transition. The absorption of the continuum states is enhanced by the so-called Sommerfeld factor. The corresponding optical absorption spectra are shown Fig. 2 for bound and continuum states considering different

dielectric constants to highlight screening effects. Experimental absorption spectra below 159 K and above 212 K are well reproduced with effective dielectric constants of 11 and 20, respectively (Fig. 2). These values may be compared to the dielectric constants available in the literature for $CH_3NH_3PbI_3$ and $CH_3NH_3PbCl_3$ summarized in Supplementary Table S7 (see also Supplementary for additional discussion). Available data evidence different features for the high and low frequency regimes as sketched Fig. 3. First, the high frequency behaviour can be related to vibrational polar phonons of the lattice by analogy with reflectivity measurements on the all-inorganic analogue $CsPbCl_3$[38]. From comparison of dielectric measurements at 1KHz (Ref. 28) and millimeter wave spectroscopy at 90GHz (ref. 40), we conclude that the high frequency vibrational contributions are little affected by the phase transition in $CH_3NH_3PbX_3$. Next, an additional contribution shows up above T_c in the low frequency range (Fig. 3). We attribute this dielectric increment to the collective tumbling of cation's C-N axis at RT, evidenced by NMR[29], dielectric[28] and millimeter wave spectroscopies[27]. A similar drop in the dielectric spectra of alkali-cyanides has been reported and related to the collective tumbling of $C\text{-}N^-$ anions that get frozen in the LT phase[39]. In C60 fullerenes, the self-localized exciton observed at LT becomes a diffusing free exciton above a critical temperature where free rotations of C60 molecules are collectively activated[40]. In $C_5H_{10}NH_2PbI_3$, a 1D hybrid perovskite, strongly bound excitons are formed, the exciton being self-trapped by deforming the lattice in its neighbourhood[41], but with a clear Stokes shift (1.2eV) which is not observed in 3D compounds like $CH_3NH_3PbI_3$. It is worth mentioning that among the all-inorganic perovskites $CsPbX_3$, $CsPbI_3$ is the only one exhibiting a self-trapped exciton at LT with a sizeable Stokes shift (0.74eV)[42]. In addition, our simulated absorption spectra (Fig. 2) indicate that the effective dielectric constant is somewhat larger then its high frequency limit ($\varepsilon_\infty \approx 6.5$) below T_c, suggesting possible exciton screening by polar

modes. For $CH_3NH_3PbX_3$, we can thus conclude that the LT exciton resonance is related to a Wannier like exciton that becomes almost completely screened above T_c, when the orientational motions of the cations are collectively activated by a structural phase transition.

In the cubic $CH_3NH_3PbX_3$ hybrid perovskites, each $CH_3NH_3^+$ cation is located in a cuboctahedral cage formed by the 12 nearest halogen atoms. The size of this cage reduces when iodine is substituted by chlorine (-25%), leading to restricted molecular motion[27]. Thus, the drop in dielectric constant is larger for iodine-based compounds. It shows up in different Lorentz local field factors evidencing the different dielectric environments in both compounds[27]. A similar variation of cell volume is observed between KCN and NaCN crystals, with a smaller cell for the latter[43]. The different behaviour of the reorientation dynamics of CN^- between these two alkali-cyanides has been attributed to both the smaller size of the NaCN lattice and to reduced polarizability for Na^+ as compared to K^+. Moreover, it has been shown that the CN^- collective ordering is severely affected by insertion of alkali metals of another size. The cationic impurities strongly hinder rotation of CN^- ions that are prevented to take part in the collective process. A comparable effect is expected upon halogen doping in 3D hybrid perovskites. If collective tumbling of $CH_3NH_3^+$ is hampered, exciton screening will be reduced leading to a sizeable increase in absorption. Such enhancement of absorption upon Cl doping has been evidenced in $CH_3NH_3PbI_3$ (ref. 21, 24) and $CH_3NH_3PbBr_3$ (ref. 44).

We can further speculate that the molecular motions that affect electron-hole interactions have also a dramatic effect on carrier mobility. At high temperature ($T>T_c$), tumbling of $CH_3NH_3^+$ cations may couple to the displacements of charge carriers in the perovskite crystal. Indeed, at RT current-voltage characteristics of $CH_3NH_3PbI_3$ exhibit a ferroelectric hysteresis attributed to the reorientation of the permanent dipoles of $CH_3NH_3^+$ on application of an external

electric field in addition to the resistance of the inorganic lattice[30]. Polarization measurements and analysis of the coercive field in the current-voltage hysteresis loops are also in favour of charge motion within the material[30]. All these results lead us to suggest a picture where carriers correspond to dressed quasiparticules, the dressing stemming from interaction with neighbouring cations that rotate so as to adiabatically follow the quasiparticule moving through the medium. Fig. 4 shows an artist view of a hole travelling through $CH_3NH_3PbI_3$. This reminds a so-called rotational polaron[45,46] but, to the best of our knowledge, models including rotational degrees of freedom have not yet been fully worked out for transport properties. In particular, no expression for the effective mass is available and we proceed by analogy with the Fröhlich-polaron theory[47], developed for optical phonons in semiconductors. Under this assumption, a decrease of the static dielectric constant, subsequent to inhibition of molecular rotation (Fig. 3), will in turn increase carrier's effective mass. The restricted rotation of the $CH_3NH_3^+$ due to chlorine doping is consistent with the increased electron-hole diffusion lengths reported for $CH_3NH_3PbI_{3-x}Cl_x$ as compared to $CH_3NH_3PbI_3$ (ref. 14, 24). The morphology of hybrid perovskite grains is also important for transport properties. Intergranular barriers, rather than intrinsic mechanisms probably dominate carrier transport in highly disordered samples and different grain sizes may result from alloys in such compounds. However, in high quality samples substantial charge carrier mobility losses at grain boundaries do not prevail[24].

In the search for environmental friendly materials for photovoltaics, we analyse the impact of metal substitution. First, $CH_3NH_3MX_3$ crystals have been reported to undergo phase transitions and do not systematically crystallize in a cubic phase at RT (ref. 27,30). For example, RT phases of $CH_3NH_3MI_3$ (M=Pb and Sn) are tetragonal (I4cm and P4mm, respectively)[30]. Supplementary Fig. S5 shows the computed absorption spectra for light polarized perpendicular and parallel to

the tetragonal axis of these structures, and the corresponding spectra of the cubic structures. Band to band optical absorptions are indeed anisotropic in the tetragonal phases, but remain comparable to those obtained for the cubic one. Besides anisotropy, these absorption spectra show comparable light-harvesting capabilities for M=Pb and Sn (see Supplementary Informations for comment on calculated bandgaps). We further investigate metal substitution for chlorine-based perovskites. Optical absorption spectra of $CH_3NH_3MCl_3$ (M=Pb, Sn, Ge) in their high temperature Pm3m cubic phases are shown Fig. 5 (calculated band structures are given as Supplementary Materials Fig. S7-S8). These calculated optical absorption spectra suggest attractive light-harvesting abilities for both $CH_3NH_3SnCl_3$ and $CH_3NH_3GeCl_3$, i.e. comparable to those obtained for the RT phase of $CH_3NH_3PbCl_3$. But, the large experimental bandgaps obtained with X=Cl, of 3.1 and 3.7 eV for M=Pb (ref. 35) and M=Sn (ref. 48) respectively, are not favourable for PV technologies based on pure materials. On the other hand, the experimental bandgap of $CH_3NH_3SnI_3$ at RT drops to 1.2 eV (ref. 24) close to the 1.5 eV measured for M=Pb (ref. 4). Since mixed-halides have proved their efficiencies for lead-based hybrids, this strategy can be extended to tin-based materials. While the possibility to build solid solutions of $CH_3NH_3SnI_{3-x}Cl_x$ was unsuccessful[49], $CH_3NH_3SnI_{3-x}Br_x$ may be an interesting alternative. In fact, for its all-bromide analogue (Supplementary Materials Fig. S9), the experimental bandgap amounts to 2.15 eV (ref. 48), and both bromine and iodine tin-based hybrids are reported to crystallize in a cubic phase at RT[48,49].

In summary, this work indicates that the broad light-harvesting abilities of the inorganic-organic family of perovskites $CH_3NH_3MX_3$, recently used for high-performance solar cells, is a direct consequence of their intrinsic multi-bandgap and multi-valley nature. In some sense, they can be thought as natural multi-junction. Inspection of the dielectric responses over a wide

frequency range allows clarifying the nature of the photoexcited species created in these materials. In particular, the Wannier-like exciton evidenced at low temperature becomes almost entirely screened at room temperature, due to collective rotational motion of the organic cations. In mixed-halides perovskites, the insertion of a halide of another size is expected to prevent such collective reorientations, thus reducing exciton screening and enhancing optical absorption. We further suggest that at ambient conditions, charge carriers are rotational polarons, i. e. quasiparticules dressed by the reorientation of neighbouring cations. This picture is also consistent with the counterintuitive increase of carrier mobility experimentally evidenced upon doping[14,24]. In fact, the disorder brought by alloying should reduce electron-hole diffusion lengths. But, doping restricts molecular motion and subsequently lowers carrier's effective mass, leading to improved transport properties. Tin based mixed-halides ($CH_3NH_3SnI_{3-x}Br_x$) are also suggested as a less toxic but potentially efficient alternative to lead-based perovskites. We believe that the past research effort invested in the field of solid state physics and conventional semiconductors provides forefront concepts and tools to further unravel our understanding of this new class of photovoltaic materials.

References

1. Shockley, W. & Queisser, H. J. Detailed balance limit of efficiency of p-n junction solar cells. *J. Appl. Phys.* **32**, 510-519 (1961).

2. Green, M. A., Emery, K., Hishikawa, Y., Warta, W. & Dunlop, E.D. Solar cell efficiency tables (version 42). *Prog. Photovolt: Res. Appl.* **21**, 827–837 (2013).

3. Friedman, D.J. Progress and challenges for next-generation high-efficiency multijunction solar cells, *Current Opinion in Solid State and Materials Science* **14**, 131-138 (2010).

4. Kojima, A., Teshima, K., Shirai, Y. & Miyasaka T. Organometal halide perovskites as visible-light sensitizers for photovoltaic cells. *J. Am. Chem. Soc.* **131**, 6050-6051 (2009).

5. Lee, M. M., Teuscher, J., Miyasaka, T., Murakami, T. N. & Snaith, H. J. Efficient hybrid solar cells based on meso-superstructured organometal halide perovskites. *Science*. **338**, 643-647 (2012).

6. Kim, H-S. *et al.* Lead iodide perovskite sensitized all-solid-state submicron thin film mesoscopic solar cell with efficiency exceeding 9%. *Sci. Rep.* **2**, 591-1-591-7 (2012).

7. Heo, J. H. *et al.* Efficient inorganic–organic hybrid heterojunction solar cells containing perovskite compound and polymeric hole conductors. *Nature Photonics*. **7**, 486-491 (2013).

8. Burschka, J. *et al.* Sequential deposition as a route to high-performance perovskite-sensitized solar cells. *Nature*. **499**, 316-319 (2013).

9. Kim, H.-S. *et al.* Mechanism of carrier accumulation in perovskite thin-absorber solar cells. *Nature Comm.* **4**, 2242 (2013).

10. Park, N. G. Organometal perovskite light absorbers toward a 20% efficiency low-cost solid-state mesoscopic solar cell. *J. Phys Chem. Lett.* **4**, 2423-2429 (2013).

11. Noh, J. H., Im, S. H., Heo, J. H., Mandal, T. N. & Seok, S. I. Chemical management for colorful, efficient, and stable inorganic–organic hybrid nanostructured solar cells. *Nano Lett.* **13**, 1764-1769 (2013).

12. Liu, M., Johnston, M. B. & Snaith, H. J. Efficient planar heterojunction perovskite solar cells by vapour deposition. *Nature.* **501**, 395-398 (2013).

13. Snaith, H. J. Perovskites: The emergence of a new era for low-cost, high-efficiency solar cells. *J. Phys Chem. Lett.* **4**, 3623-3630 (2013).

14. Stranks, S. D. *et al.* Electron-hole diffusion lengths exceeding 1 micrometer in an organometal trihalide perovskite absorber. *Science*. **342**, 341-344 (2013).

15. Xing, G. *et al.* Long-range balanced electron- and hole-transport lengths in organic-inorganic $CH_3NH_3PbI_3$. *Science*. **342**, 344-347 (2013).

16. Antonietta, M. & Hummelen, J. C. Hybrid solar cells: Perovskites under the sun. *Nature Mater.* **12**, 1087-1089 (2013).

17. Even, J., Pedesseau, L., Jancu, J.-M. & Katan, C. Importance of spin–orbit coupling in hybrid organic/inorganic perovskites for photovoltaic applications. *J. Phys. Chem. Lett.* **4**, 2999-3005 (2013).

18. Even, J., Pedesseau, L., Jancu, J.-M. & Katan, C. DFT and k · p modelling of the phase transitions of lead and tin halide perovskites for photovoltaic cells. *Phys. Status Solidi RRL*. **8**, 31–35 (2014).

19. Brivio, F., Walker, A. B. & Walsh, A. Structural and electronic properties of hybrid perovskites for high-efficiency thin-film photovoltaics from first-principles. *Appl. Phys. Lett. Mat.* **1**, 042111-1-042111-5 (2013).

20. Baikie, T. *et al.* Synthesis and crystal chemistry of the hybrid perovskite $(CH_3NH_3)PbI_3$ for solid-state sensitised solar cell applications. *J. Mater. Chem. A*. **1**, 5628-5641 (2013).

21. Colella, S. *et al.* $MAPbI_{3-x}Cl_x$ mixed halide perovskite for hybrid solar cells: The role of chloride as dopant on the transport and structural properties. *Chem. Mater.* **25**, 4613-4618 (2013).

22. Mosconi, E., Amat, A., Nazeeruddin, Md. K., Grätzel, M. & De Angelis, F. First-principles modeling of mixed halide organometal perovskites for photovoltaic applications. *J. Phys. Chem. C* **117**, 13902-13913 (2013).

23. Giorgi, V., Fujisawa, J.-I., Segawa, H. & Yamashita, K. Small photocarrier effective masses featuring ambipolar transport in methylammonium lead iodide perovskite: A density functional analysis. *J. Phys. Chem. Lett.* **4**, 4213-4216 (2013).

24. Wehrenfennig, C., Eperon, G. E., Johnston, M. B., Snaith, H. J., & Herz, L. M. High charge carrier mobilities and lifetimes in organolead trihalide perovskites. *Adv. Mat.* (2014) DOI: 10.1002/adma.201305172

25. Saurat, M. & Ritthoff, M. Photovoltaics and the RoHS directive, Position Paper, Wuppertal Institute for Climate, Environment and Energy. May 2010.

26. Ishihara, T. Optical properties of PbI-based perovskite structures, *J. of Lum.,* **60&61**, 269-274 (1994).

27. Poglitsch, A. & Weber, D. Dynamic disorder in methylammoniumtrihalogenoplumbates (II) observed by millimeter‐wave spectroscopy. *J. Chem. Phys.* **87**, 6373-6378 (1987).

28. Onoda-Yamamuro, N., Matsuo, T. & Suga, H., Dielectric study of CH_3,NH_3PbX_3 (X = Cl, Br, I). *J. Phys. Chem. Solids,* **53**, 935-939 (1992).

29. Wasylishen, R. E., Knop, O., & Macdonald, J. B., Cation rotation in methylammoniumlead halides. *Solid State Comm.*, 56, 581-582 (1985).

30. Stoumpos, C. C., Malliakas, C. D. & Kanatzidis, M. G. Semiconducting tin and lead iodide perovskites with organic cations: Phase transitions, high mobilities, and near-infrared photoluminescent properties. *Inorg. Chem.* **52**, 9019-9038 (2013).

31. Even, J., Pedesseau, L., Dupertuis, M.-A., Jancu, J.-M. & Katan, C. Electronic model for self-assembled hybrid organic/perovskite semiconductors: Reverse band edge electronic states ordering and spin-orbit coupling. *Phys. Rev. B*. **86**, 205301-1-205301-4 (2012).

32. Ferreira, R. & Bastard, G. Phonon-assisted capture and intradot Auger relaxation in quantum dots. *Appl. Phys. Lett.* **74**, 2818-2820 (1999).

33. Miska, P., Even, J., Marie, X. & Dehaese, O. Electronic structure and carrier dynamics in InAs/InP double-cap quantum dots. *Appl. Phys. Lett.* **94**, 061916-1-061916-3 (2009).

34. Hirasawa, M., Ishihara, T. & Goto, T. Exciton Features in 0-, 2-, and 3-Dimensional Networks of $[PbI_6]^{4-}$ Octahedra. *J. Phys. Soc. Jpn.* **63**, 3870-3879 (1994).

35. Kitazawa, N., Watanabe, Y. & Nakamura, Y. Optical properties of $CH_3NH_3PbX_3$ (X = halogen) and their mixed-halide crystals. *J. Mat. Sci.* **37**, 3585-3587 (2002).

36. Pedesseau, L., Jancu, J-M., Rolland, A., Deleporte, E., Katan, C. & Even, J. Electronic properties of 2D and 3D hybrid organic/inorganic perovskites for optoelectronic and photovoltaic applications. *Opt. Quant. Electron.* (2013), DOI: 10.1007/s11082-013-9823-9

37. Chuang, S. Physics of Optoelectronic Devices. (J. W. Goodman Ed., New York: Wiley, 1995).

38. Hirotsu, S. Far-infrared reflectivity specra of $CsPbCl_3$. *Phys. Lett. A* **41**, 55-56 (1972).

39. Ortiz-Lopez, J. Dipolar Reorientation and Order-Disorder Behavior of Pure and Mixed Alkali Cyanides. *Phys. Rev. Lett.* **50**, 1289–1292 (1983).

40. M. Matus, M., Kuzmany, H. Sohmen, E. Self-Trapped Polaron Exciton in Neutral Fullerene C60. *Phys. Rev. Lett.* **68**, 2822-2825 (1992).

41. Nagami, A., Okamura, K. & Ishihara, T. Optical properties of a quantum wire crystal, $C_5H_{10}NH_2PbI_3$. *Physica B* **227**, 346-348 (1996).

42. Nikl, M., Nitsch, K., Chval, J., Somma, F., Phani, A. R., Santucci, S., Giampaolo, C., Fabeni, P., Pazzi, G. P. & Feng, X. Q. Optical and structural properties of ternary nanoaggregates in CsI–PbI_2 co-evaporated thin films. *J. Phys.: Condens. Matter* **12**, 1939–1946 (2000).

43. Ortiz-Lopez, J. & Lüty, F. Dielectric Studies of CN^- Dipolar Reorientation and Order–Disorder Behavior in $RbCN_{1-x}$:KCN_x and KCN_{1-x}:$NaCN_x$. *Phys. status solidi (b)* **228**, 893–917 (2001).

44. Edri, E., Kirmayer, S., Kulbak, M., Hodes, G. & Cahen, D. Chloride Inclusion and Hole Transport Material Doping to Improve Methyl Ammonium Lead Bromide Perovskite-Based High Open-Circuit Voltage Solar Cells. *J. Phys. Chem. Lett.* (2014) DOI: 10.1021/jz402706q

45. Kenkre, V. M. What do polarons owe to their harmonic origins? *Physica D* **113**, 233-241 (1998).

46. Zhang, W., Govorov, A. O. & Ulloa, S. E. Polarons with a twist. *Phys. Rev. B* **66**, 060303(R) (2002).

47. Devreese, J. T. Fröhlich polarons from 0D to 3D: concepts and recent developments. *J. Phys.: Condens. Matter* **19**, 255201 (2007)

48. Chiarella, F., Zappettini, A. & Licci, F. Combined experimental and theoretical investigation of optical, structural, and electronic properties of $CH_3NH_3SnX_3$ thin films (X=Cl,Br). *Phys. Rev. B*. **77**, 045129-1-045129-6 (2008).

49. Yamada, K., Nakada, K., Takeuchi, Y., Nawa, K. & Yamane, Y. Tunable perovskite semiconductor $CH_3NH_3SnX_3$ (X: Cl, Br, or I) characterized by X-ray and DTA. *Bull. Chem. Soc. Jpn*. **84**, 926-932 (2011).

Supplementary Information is linked to the online version of the paper at http://www.nature.com/nmat.

Acknowledgments This work was performed using HPC resources from GENCI-CINES/IDRIS grant 2013-c2013096724. The work is supported by Agence Nationale pour la Recherche (PEROCAI project ANR-10-04).

Author contributions J.E. guided the work. J.E and L.P. carried out the ab-initio calculations. J.E. and C.K. provided the theoretical description of the hybrid perovskites, discussed the results and wrote the manuscript.

Author Information Reprints and permissions information is available at http://www.nature.com/reprints. The authors declare no competing financial interests. Readers are welcome to comment on the online version of the paper. Correspondence and requests for materials should be addressed to J. E. (jacky.even@insa-rennes.fr) or to C. K. (Claudine.Katan@univ-rennes1.fr)

Figure Legends

Figure 1. Analysis of optical absorption spectra of $CH_3NH_3MX_3$ based on group theory, electronic band diagram and Fermi surface. a, Real space 3D view of the Pm3m cubic crystal structure of metal-halide hybrid perovskites of general formulae $CH_3NH_3MX_3$. The $CH_3NH_3^+$ cation is located at the center of the cube with an averaged position sketched by a red ball. **b**, Reciprocal space 3D view showing the first Brillouin Zone (BZ) of the Pm3m space group. Points of high symmetry in the cubic BZ are indicated by conventional letters: Γ denotes the origin of the BZ; X is the center of a square face at the BZ boundary, M is a center of a cube edge; and R are vertices of the cube. **c**, Schematic energy levels diagrams drawn at the high symmetry R and M points of the Pm3m BZ. Irreducible representations of the simple (SOC=0, where SOC denotes spin orbit coupling) and double (SOC≠0) groups are indicated. The level splitting associated to SOC are labeled Δ_g^R, Δ_u^R and Δ_u^M. The additional spin degeneracy is not indicated for the double group representations. The upward arrows show the symmetry allowed optical transitions. **d**, Electronic band diagram of the high temperature Pm3m cubic phase of $CH_3NH_3PbI_3$ taking SOC into account; an upward energy shift of 1.4eV has been applied to match the experimental bandgap value at R. Carrier localization and transport after optical excitation are sketched. **e**, Fermi surface (E=-0.5eV) in the first BZ. R and M are connected along the edges, highlighting the saddle point nature of M.

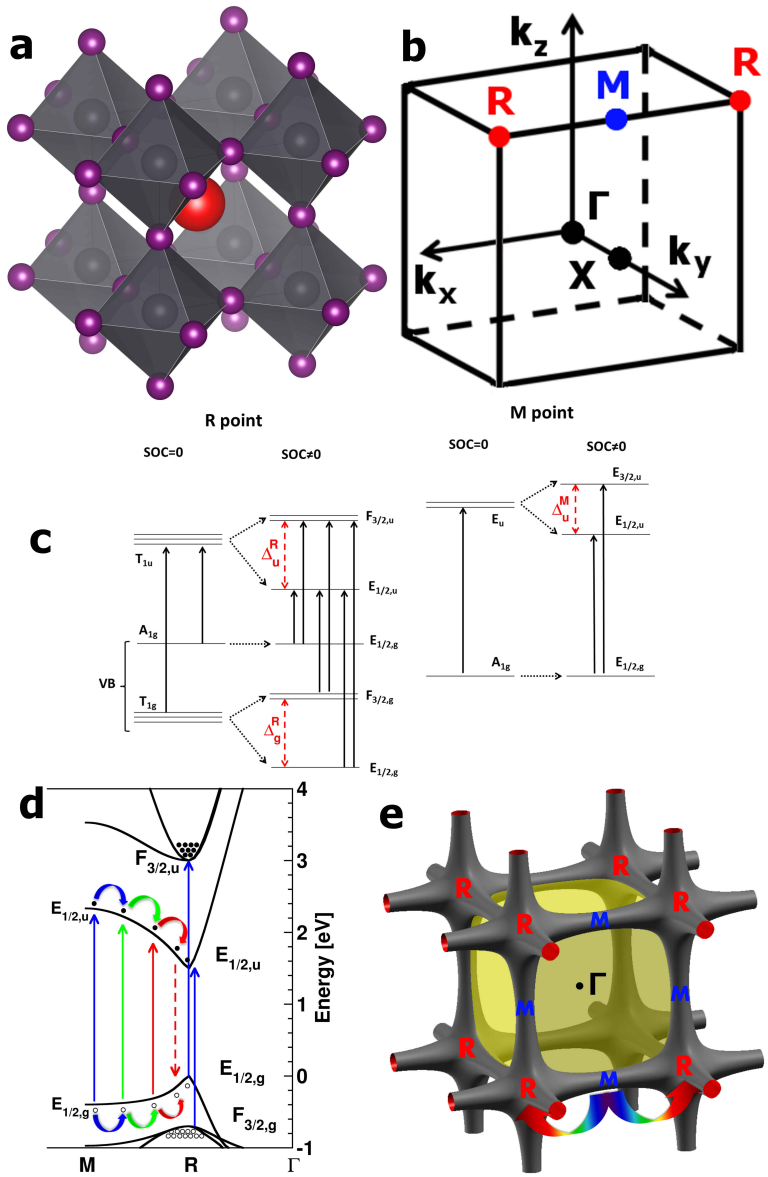

Figure 1. Analysis of optical absorption spectra of $CH_3NH_3MX_3$ based on group theory, electronic band diagram and Fermi surface. a, Real space 3D view of the Pm3m cubic crystal structure of metal-halide hybrid perovskites of general formulae $CH_3NH_3MX_3$. The $CH_3NH_3^+$ cation is located at the center of the cube with an averaged position sketched by a red ball. **b**, Reciprocal space 3D view showing the first Brillouin Zone (BZ) of the Pm3m space group. Points of high symmetry in the cubic BZ are indicated by conventional letters: Γ denotes the origin of the BZ; X is the center of a square face at the BZ boundary, M is a center of a cube edge; and R are vertices of the cube. **c**, Schematic energy levels diagrams drawn at the high symmetry R and M points of the Pm3m BZ. Irreducible representations of the simple (SOC=0, where SOC denotes spin orbit coupling) and double (SOC≠0) groups are indicated. The level splitting associated to SOC are labeled Δ_g^R, Δ_u^R and Δ_u^M. The additional spin degeneracy is not indicated for the double group representations. The upward arrows show the symmetry allowed optical transitions. **d**, Electronic band diagram of the high temperature Pm3m cubic phase of $CH_3NH_3PbI_3$ taking SOC into account; an upward energy shift of 1.4eV has been applied to match the experimental bandgap value at R. Carrier localization and transport after optical excitation are sketched. **e**, Fermi surface (E=-0.5eV) in the first BZ. R and M are connected along the edges, highlighting the saddle point nature of M.

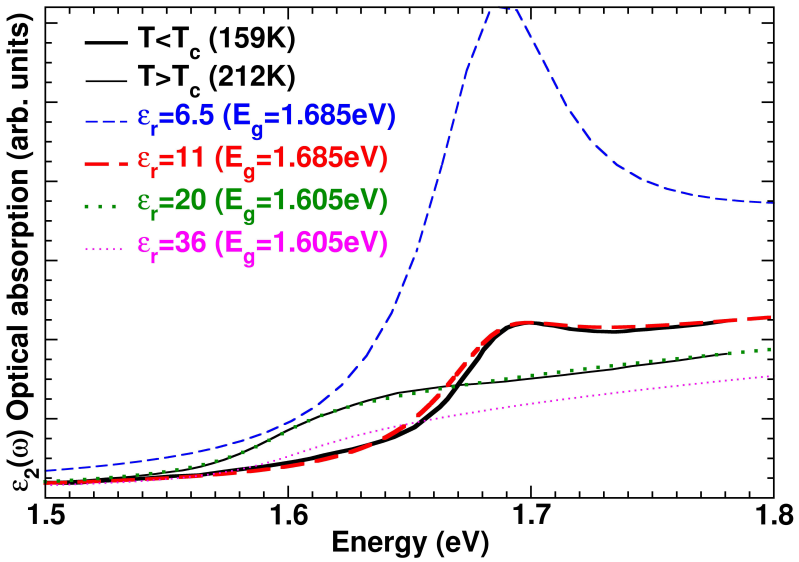

Figure 2. Optical absorption spectra of $CH_3NH_3PbI_3$ highlighting exciton screening. Experimental data taken from Ref. 26 recorded at 159 K (black thick line) and 212 K (black thin line) and computed spectra for bound and continuum states, considering two-particle wave function and effective mass equations for electron and hole[37]. A damping factor of 0.1eV has been used. Various effective dielectric constants (ε_r) illustrate the effect of dielectric screening. ε_r=11 (red dash line) and 20 (green dot line) lead to the best fit of the experimental spectra below (159K) and above T_c (212K), respectively.

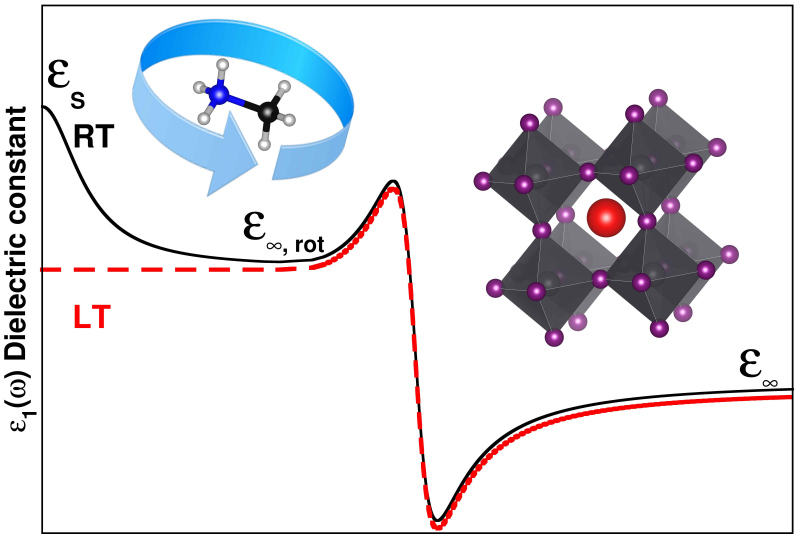

Figure 3. Schematic drawing of the dielectric constant as a function of frequency displaying respective contributions of $CH_3NH_3^+$ rotations and perovskite's vibrational phonons. Frequency dependence of the dielectric constant of $CH_3NH_3PbX_3$ as derived from available experimental data summarized in Supplementary Table S7. The high frequency response is related to vibrational polar phonons stemming from modes of the perovskite lattice (right hand side). The low frequency region (left hand side) shows significant differences for the low (LT, red dash line) and room (RT, black line) temperature phases. The static dielectric constant (ε_S) increase at RT is primarily attributed to rotational motion of $CH_3NH_3^+$ cations.

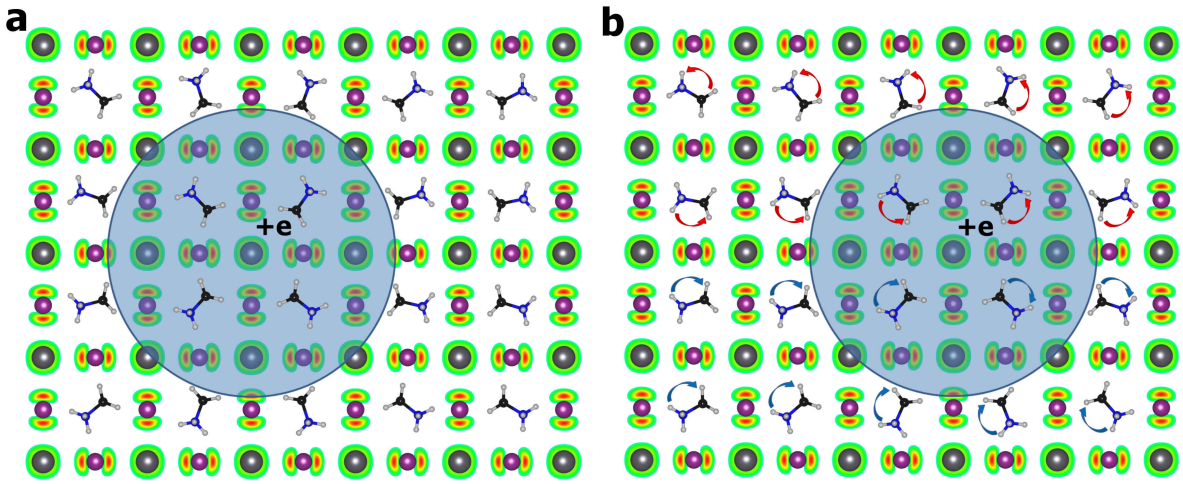

Figure 4. Artist view of a quasiparticle hole dressed by the interaction with neighbouring rotating cations and travelling across the crystal. **a,** Quasiparticule hole starting from the left part of the cubic lattice ((a,b) plane) of the $CH_3NH_3PbX_3$ crystal surrounded by $CH_3NH_3^+$ cations that gear around the quasiparticule, forming a so-called rotating polaron. **b,** Adiabatic collective rotation of the cations when the quasiparticule hole moves to the right part of the medium.

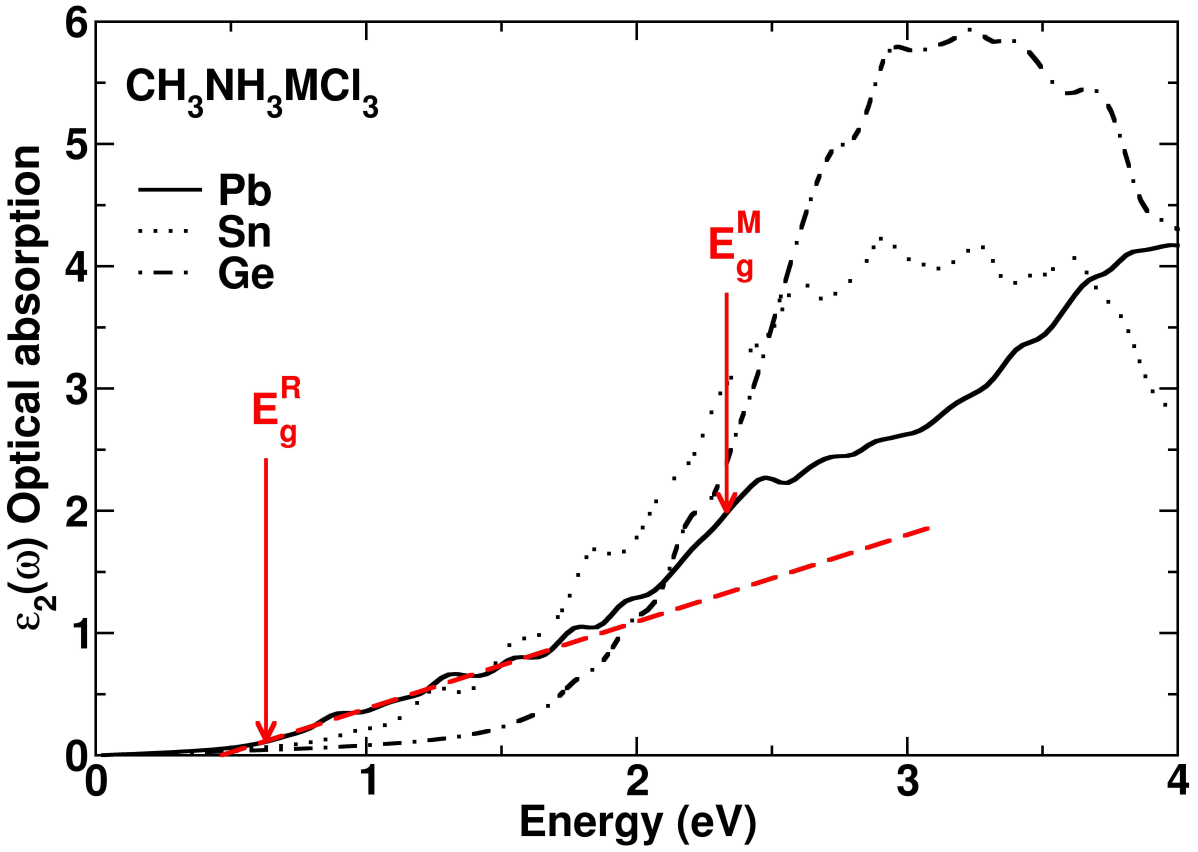

Figure 5. Effect of metal substitution on the absorption spectra illustrated for $CH_3NH_3MCl_3$ (M=Pb, Sn, Ge). Absorption spectra calculated for the high temperature cubic structures of $CH_3NH_3MCl_3$ (M=Pb, Sn, Ge). Onsets of optical absorption at R and M are indicated for $CH_3NH_3PbCl_3$. Corresponding figure calculated without spin orbit coupling available as Supplementary Fig. S6.